Signature of Arctic first-year ice melt pond fraction in X-band SAR imagery

Ane S. Fors[1], Dmitry V. Divine[2], Anthony P. Doulgeris[1], Angelika H. H. Renner[2,3], and Sebastian Gerland[2]

[1]Department of Physics and Technology, University of Tromsø - The Arctic University of Norway, 9037 Tromsø, Norway
[2]Norwegian Polar Institute, FRAM Centre, 9296 Tromsø, Norway
[3]Institute of Marine Research, 9294 Tromsø, Norway

Correspondence to: Ane Fors (ane.s.fors@uit.no)

Abstract. In this paper we investigate the potential of melt pond fraction retrieval from X-band polarimetric synthetic aperture radar (SAR) on drifting first-year sea ice. Melt pond fractions retrieved from a helicopter-borne camera system were compared to polarimetric features extracted from four dual polarimetric X-band SAR scenes, revealing significant relationships. The correlations were strongly dependent on wind speed and SAR incidence angle. Co-polarisation ratio was found to be the most promising SAR feature for melt pond fraction estimation at intermediate wind speeds (6.2 m/s), with a correlation coefficient of 0.46. At low wind speeds (0.6 m/s), this relation disappeared due to low backscatter from the melt ponds, and backscatter VV-polarisation intensity had the strongest relationship to melt pond fraction with a correlation coefficient of −0.53. From the results, an intermediate and a low-wind speed empirical model for melt pond fraction estimation were suggested and evaluated. The models gave good estimates of mean melt pond fraction for the full satellite scenes, deviating with less than 4% from the airborne retrieved melt pond fractions in the investigated area. A smoothing window of 51×51 pixels gave the best reproduction of the width of the melt pond fraction distribution. A considerable part of the backscatter signal was below the noise floor at SAR incidence angles above $\sim 40°$, restricting the information gain from polarimetric features above this threshold. Compared to previous studies in C-band, limitations concerning wind speed and noise floor set stricter constraints on melt pond fraction retrieval in X-band. Despite this, our findings demonstrate new possibilities in melt pond fraction estimation from SAR, opening for expanded monitoring of melt ponds during melt season. In the next step, melt pond estimation from SAR may supplement surveillance from optical satellites, providing melt pond information to climate applications during cloudy conditions.

1 Introduction

Melt ponds form from snow and ice melt water on the Arctic sea ice during spring and summer, and can cover up to $50 - 60\%$ of the sea ice surface (Perovich, 2002; Eicken et al., 2004; Inoue et al.,
25   2008; Perovich et al., 2009; Polashenski et al., 2012). Their presence affects the heat budget of the sea ice by decreasing the surface albedo, which increases the solar absorption in the ice volume and the transmission of solar energy to the ocean (Eicken et al., 2004; Ehn et al., 2011; Nicolaus et al., 2012; Perovich and Polashenski, 2012). The transmission is generally larger for first-year ice (FYI) than for multiyear ice (MYI) due to FYI's lower sea ice thickness. (Light et al., 2008; Nicolaus et al.,
30   2012; Hudson et al., 2013). FYI also often experiences higher melt pond fractions (f_{MP}) than MYI (Fetterer and Untersteiner, 1998; Nicolaus et al., 2012). The increased absorption induced by melt ponds accelerates the decay of sea ice, and the intensified warming of the ocean possibly delays the ice growth in the autumn (Flocco et al., 2012; Holland et al., 2012; Hudson et al., 2013; Schröder et al., 2014; Flocco et al., 2015). Formation and evolution of melt ponds are poorly represented in sea
35   ice models, potentially contributing to an underestimation of the observed sea ice extent reduction in model projections (Flocco et al., 2012; Holland et al., 2012; Flocco et al., 2015). An increased number of observations of melt pond fraction (f_{MP}) for different sea ice types at regional scale is needed to improve the understanding of the role of melt ponds in the Arctic climate system. Satellite imagery offers good opportunities for such large scale monitoring of melt ponds.

40   Several algorithms have been developed for retrieval of melt pond fraction from optical satellites, measuring the spectral reflectance from open water, sea ice and melt ponds. The algorithms apply to different multispectral sensors; the enhanced thematic mapper plus (ETM+) on board Landsat 7 (Markus et al., 2003; Rösel and Kaleschke, 2011), moderate-resolution imaging spectroradiometer (MODIS) on board Aqua and Terra (Tschudi et al., 2008; Rösel et al., 2012; Rösel and Kaleschke,
45   2012), and medium resolution imaging spectrometer (MERIS) on board Envisat (Zege et al., 2015; Istomina et al., 2015). Commonly, the retrieval algorithms are vulnerable to correction for atmospheric constituents and influences of the viewing angles and the solar geometry. They also require cloud-free conditions, limiting their applicability in the Arctic due to the persistent cloud cover present during summer. Satellite microwave radiometers and scatterometers can on the other hand
50   penetrate clouds, but their resolution is in general too coarse for automated melt pond monitoring (Comiso and Kwok, 1996; Howell et al., 2006).

Satellite synthetic aperture radar (SAR) offers independence of cloud cover, atmospheric constituents, and daylight, combined with high spatial resolution. Several studies have focused on f_{MP} retrieval from single polarisation SAR, transmitting and receiving either vertical (VV) or horizontal
55   (HH) polarised waves. Jeffries et al. (1997) developed a model for f_{MP} retrieval over MYI floes in the Beaufort sea from ERS-1 SAR satellite images, but lack of wind consideration limit the validity of the model. Wind speed was found to be a key parameter when Yackel and Barber (2000) demonstrated a significant relation between f_{MP} and HH intensity on land-fast FYI within the Cana-

dian Arctic Archipelago using SAR satellite scenes from Radarsat-1. The relationship was strong at
60   intermediate wind speeds, but lacking at low wind speeds. Mäkynen et al. (2014) compared f_{MP}
retrieved from MODIS and from a large amount of ENVISAT ASAR satellite scenes. The study
area covered both FYI and MYI north of the Fram Strait. The study concluded that f_{MP} estima-
tion was not possible based on the investigated data set. The above-mentioned studies all focus on
C-band frequency (5.4 GHz) SAR. Kern et al. (2010) investigated the use of supplementary fre-
65   quencies for f_{MP} retrieval on MYI in the Arctic Ocean, and showed promising results in combining
C, Ku (17.2 GHz) and X (9.6 GHz) band data from a helicopter-borne scatterometer. Estimation of
f_{MP} in X-band satellite SAR was further explored by Kim et al. (2013), investigating melt ponds
in a TerraSAR-X scene acquired over MYI in the Chukchi Sea. Only large melt ponds were found
possible to detect in the study, leading to an underestimation of f_{MP}.

70   Dual and quad polarimetric SAR transmit and receive both vertical and horizontal waves, result-
ing in four possible channel combinations (HH, HV, VH and VV), and give information about the
polarisation properties of the backscatter in addition to single channel intensity variations. The chan-
nels can be combined into polarimetric SAR features, e.g. channel ratios, reducing the dependency
of sensor geometry. Based on C-band scatterometer measurements, Scharien et al. (2012) suggested
75   co-polarisation ratio ($R_{VV/HH}$) to give an unambiguous estimation of f_{MP} at large incidence angles
for land-fast FYI in the Canadian Arctic Archipelago and the Beaufort Sea. The topic was further
investigated (Scharien et al., 2014b), and expanded to Radarsat-2 satellite scenes in Scharien et al.
(2014a), demonstrating a strong potential of f_{MP} estimation from C-band dual polarimetric space-
borne SAR. Both studies were performed in the central Canadian Arctic Archipelago. The findings
80   were partly confirmed by Fors et al. (2015), who also suggest a relationship between f_{MP} and the
statistical SAR feature relative kurtosis (RK) utilizing Radarsat-2 on iceberg-fast FYI and MYI in
the Fram Strait. Han et al. (2016) combined multiple polarimetric SAR features for f_{MP} estimation,
employing the co-polarisation channels of the X-band SAR scene explored in Kim et al. (2013). The
study showed promising results, but more scenes, a broader range of melt pond fractions, and inclu-
85   sion of wind information are needed to confirm the findings. In summary, the main achievements on
f_{MP} retrieval with SAR come from C-band studies on land-fast FYI or MYI. Few studies have in-
vestigated other frequencies, and little attention has been paid to drifting FYI, an ice type becoming
more prominent in the Arctic with the recent shift to a thinner, more seasonal, and more mobile sea
ice cover (Perovich et al., 2015).

90   The objective of this study is to investigate the potential of melt pond fraction retrieval from
drifting FYI with dual polarimetric X-band satellite SAR. A data set consisting of four high res-
olution dual-polarisation TerraSAR-X satellite scenes, combined with melt pond fraction retrieved
from a helicopter-borne camera system forms the basis of the study. The data were collected north
of Svalbard in summer 2012. We explore the correlation between f_{MP} and different polarimetric
95   SAR features extracted from the HH and VV channels. Based on the results, we suggest two simple

empirical models for f_{MP} estimation adjusted to an intermediate and a low-wind speed case. The influence and limitations related to wind conditions, incidence angle, noise floor, scale and surface roughness are discussed in light of the results.

2 Melt ponds in SAR imagery

100 The signature of melt ponds in SAR imagery depends on both melt pond properties and radar parameters. Wind at the sea ice surface changes the surface roughness of the melt ponds, and hence their SAR backscatter signature and contrast to the surrounding sea ice. The influence of wind is dependent on fetch length, depth of the ponds, orientation of the ponds and the topography of the surrounding sea ice (Scharien et al., 2012, 2014b). During very calm conditions, the SAR signal
105 of melt ponds is mainly specular. This occurs at wind speeds of $2 - 3$ m/s in 10 m height (U_{10}) in C-band, in agreement with findings for ocean surfaces (~ 2.0 m/s at $0°C$) (Donelan and Pierson, 1987; Scharien et al., 2012, 2014b). A similar threshold in X-band equals ~ 2.8 m/s (Donelan and Pierson, 1987). Refrozen ponds suppress the wind wave surface roughness induced on open ponds, and yield a signature closer to newly formed sea ice (Yackel et al., 2007; Scharien et al., 2014b, a).
110 The size distribution of melt ponds also affects their SAR signature. Ponds smaller than the SAR resolution return a signal mixed with sea ice and possibly leads, while very large melt ponds could fill a resolution cell. Choice of SAR resolution and speckle smoothing window size could hence affect the SAR f_{MP} signature.

The SAR signature of melt ponds changes with incidence angle of the satellite. Scharien et al.
115 (2012) found a larger decrease in C-band SAR intensity (σ^0) with increasing incidence angle for melt ponds than for sea ice. In contrast to sea ice, σ^0_{HH} decreased more than σ^0_{VV} for melt ponds. The most suitable incidence angle ranges for f_{MP} retrieval is method dependent. SAR frequency also influences the melt pond signature (Kern et al., 2010). Observed surface roughness increases with increasing frequency, making X-band more sensitive to small-scale surface roughness than C-
120 band. In addition, the sea ice volume penetration depth decreases with increasing frequency, leading to less volume scattering from sea ice at higher frequencies.

Several dual-polarimetric SAR features have been suggested for f_{MP} retrieval from SAR, utilizing different expected relations to physical properties of sea ice and melt ponds (Scharien et al., 2012, 2014a; Fors et al., 2015; Han et al., 2016). Six of these features are included in our study and
125 are described in the following subsection.

2.1 Polarimetric SAR features

For a fully polarimetric SAR system, which transmits and receives both horizontally (H) and vertically (V) polarised waves, the scattering matrix can be written as

$$
\boldsymbol{S} = \begin{bmatrix} S_{HH} & S_{VH} \\ S_{HV} & S_{VV} \end{bmatrix} = \begin{bmatrix} |S_{HH}|e^{j\phi_{HH}} & |S_{VH}|e^{j\phi_{VH}} \\ |S_{HV}|e^{j\phi_{HV}} & |S_{VV}|e^{j\phi_{VV}} \end{bmatrix},
\tag{1}
$$

130   where $|\cdot|$ and ϕ_{xx} denote the amplitude and the phase of the measured complex scattering coefficients, respectively (Lee and Pottier, 2009). Assuming reciprocity ($S_{HV} = S_{VH}$), the Pauli basis scattering vector, $\boldsymbol{k}$, can be extracted from $\boldsymbol{S}$ as

$$
\boldsymbol{k} = \frac{1}{\sqrt{2}} \begin{bmatrix} S_{HH} + S_{VV} & S_{HH} - S_{VV} & 2S_{HV} \end{bmatrix}^{\dagger},
\tag{2}
$$

where $\dagger$ denotes the transpose operator (Lee and Pottier, 2009). In our study, we are only utilizing
135   the co-polarisation channels (HH and VV), and so the scattering vector reduces to

$$
\boldsymbol{k} = \frac{1}{\sqrt{2}} \begin{bmatrix} S_{HH} + S_{VV} & S_{HH} - S_{VV} \end{bmatrix}^{\dagger}.
\tag{3}
$$

The sample coherency matrix, $\boldsymbol{T}$, is defined as the mean Hermitian outer product of the Pauli basis scattering vector:

$$
\boldsymbol{T} = \frac{1}{L} \sum_{i=1}^{L} \boldsymbol{k}_i \boldsymbol{k}_i^{*\dagger},
\tag{4}
$$

140   where $\boldsymbol{k}_i$ is the single-look complex vector corresponding to pixel i, L is the number of scattering vectors in a local neighborhood, and $*$ denotes the complex conjugate (Lee and Pottier, 2009). Similarly, in the dual-polarisation case, the Lexicographic basis scattering vector, $\boldsymbol{s}$, can be written as

$$
\boldsymbol{s} = \begin{bmatrix} S_{HH} & S_{VV} \end{bmatrix}^{\dagger}.
\tag{5}
$$

145   Based on $\boldsymbol{s}$, the sample covariance matrix, $\boldsymbol{C}$, is defined as

$$
\boldsymbol{C} = \frac{1}{L} \sum_{i=1}^{L} \boldsymbol{s}_i \boldsymbol{s}_i^{*\dagger},
\tag{6}
$$

where $\boldsymbol{s}_i$ is the single look complex vector corresponding to pixel i (Lee and Pottier, 2009).

The SAR intensity (σ^0) is retrieved from a single polarisation channel, defined by the amplitudes of the complex scattering coefficients,

150   $\sigma^0_{VV} = \langle |S_{VV}|^2 \rangle$ and $\sigma^0_{HH} = \langle |S_{HH}|^2 \rangle$,
\qquad(7)

were $\langle \cdot \rangle$ denotes an ensemble average. The relation between these basic features and f_{MP} have been investigated in several studies (Jeffries et al., 1997; Yackel and Barber, 2000; Mäkynen et al., 2014;

Kern et al., 2010; Kim et al., 2013). However, carrying information from one single polarisation channel only, makes them less robust than polarimetric features that hold information from several channels.

Co-polarisation ratio ($R_{VV/HH}$) has so far been the most promising SAR feature for f_{MP} extraction in C-band (Scharien et al., 2014a). It is defined as the ratio between the intensities of the co-polarisation complex scattering coefficients

$$R_{VV/HH} = \frac{\langle |S_{VV}|^2 \rangle}{\langle |S_{HH}|^2 \rangle}. \tag{8}$$

For smooth surfaces within the Bragg scatter validity region, $R_{VV/HH}$ depends only on the surface complex permittivity and local incidence angle, and is independent of surface roughness (Hajnsek et al., 2003). Both freshwater and saline melt ponds have considerably higher complex permittivity than sea ice, and $R_{VV/HH}$ has therefore been suggested for f_{MP} retrieval (Scharien et al., 2012, 2014b, a). The Bragg criterion is fulfilled for $ks_{RMS} < 0.3$, where k is the wavenumber and s_{RMS} is the root mean square height of the sea ice surface, describing its surface roughness. This corresponds to $s_{RMS} < 2.8$ mm in C-band, and $s_{RMS} < 1.4$ mm in X-band. The sea ice surface roughness was found to high to fill the criterion in studies north of Spitsbergen and in the Fram Strait (Beckers et al., 2015; Fors et al., 2016b), while Scharien et al. (2014b) found land-fast ice in the central Canadian Arctic Archipelago to fulfill the criterion at C-band, and partly at X-band. In the same study, melt ponds filled the criterion at wind speeds below 6.4 m/s in C-band, corresponding to ~ 5.5 m/s in X-band (Scharien et al., 2014b). When the Bragg criterion is exceeded, $R_{VV/HH}$ decreases with increasing surface roughness. $R_{VV/HH}$ increases with incidence angle, and Scharien et al. (2012) found incidence angles above $35°$ to be most appropriate for f_{MP} retrieval based on $R_{VV/HH}$ in C-band.

Relative kurtosis (RK) is a statistical measure of non-Gaussianity, which describes the shape of the distribution of scattering coefficients in SAR scenes. It has previously been used for sea ice segmentation (Moen et al., 2013; Fors et al., 2016a). It is defined as Mardia's multivariate kurtosis of a sample, divided by the expected multivariate kurtosis of a complex normal distribution

$$\mathrm{RK} = \frac{1}{L} \frac{1}{d(d+1)} \sum_{i=1}^{L} \left[\mathbf{s}_i^{*\dagger} \mathbf{C}^{-1} \mathbf{s}_i \right]^2, \tag{9}$$

where d is the number of polarimetric channels (Mardia, 1970; Doulgeris and Eltoft, 2010). It has a potential in f_{MP} retrieval as it is sensitive to mixtures of surfaces. At C-band, RK was found significantly correlated to f_{MP} over iceberg-fast sea ice in the Fram Strait (Fors et al., 2015).

Entropy (H) is a part of the $H/A/\overline{\alpha}$ polarimetric decomposition, based on the eigenvectors and eigenvalues of $\boldsymbol{T}$, describing SAR scattering mechanisms. H is a measure of the randomness of the scattering processes, and is defined as

$$H = -\sum_{i=1}^{d} p_i \log_d p_i, \tag{10}$$

where p_i is the relative magnitude of each eigenvalue

$$p_i = \frac{\lambda_i}{\sum_{k=1}^{d} \lambda_k}, \tag{11}$$

and λ_i is the ith eigenvalue of $\boldsymbol{T}$ ($\lambda_1 > \lambda_2$) (Cloude and Pottier, 1997). Only the co-polarisation

190 channels (HH and VV) are included in our study ($d = 2$), and a dual polarisation version of the entropy, denoted H', is therefore used (Cloude, 2007; Skrunes et al., 2014). $H' = 0$ indicates a single dominant scattering mechanism, while $H' = 1$ indicates a depolarized signal. In the case of dual polarisation, H' and anisotropy represent the same information as they both only depends on λ_1 and λ_2, and anisotropy is therefore not included in our study.

195 The alpha angle of the largest eigenvalue (α_1') describes the type of the dominating scattering mechanism. It is expressed as

$$\alpha_1' = \cos^{-1} \frac{|x_1|}{|v_1|}, \tag{12}$$

where x_1 is the first element of the largest eigenvector, and $|v_1|$ is the norm of the first eigenvector (Lee and Pottier, 2009). The feature can be written as a function of $R_{VV/HH}$ for slightly rough

200 surfaces, and will then increase with increasing complex permittivity (van Zyl and Kim, 2011).

Co-polarisation correlation magnitude ($|\rho|$) is defined as

$$|\rho| = \left| \frac{\langle S_{\mathrm{HH}} S_{\mathrm{VV}}^* \rangle}{\sqrt{\langle S_{\mathrm{HH}} S_{\mathrm{HH}}^* \rangle \langle S_{\mathrm{VV}} S_{\mathrm{VV}}^* \rangle}} \right|, \tag{13}$$

and describes the degree of correlation between the co-polarisation channels (Drinkwater et al., 1992). A perfect correlation returns unity, while depolarisation of the signal will reduce the mag-

205 nitude. Complex surfaces, multiple scattering surface layers and/or presence of system noise could depolarize the signal (Drinkwater et al., 1992).

Phase difference ($\angle\rho$) is expressed as (Drinkwater et al., 1992)

$$\angle\rho = \angle \left(\langle S_{\mathrm{HH}} S_{\mathrm{VV}}^* \rangle \right). \tag{14}$$

As the relative phase of the co-polarisation waves is changed in every scattering event, the mean and

210 standard deviation of $\angle\rho$ are related to the scattering history (Eom and Boerner, 1991; Drinkwater et al., 1992). Han et al. (2016) found H, α_1', $|\rho|$, and $\angle\rho$ to give useful information for f_{MP} retrieval at X-band.

3 Methods

3.1 Study region

215 The ICE2012 campaign took place on drifting FYI north of Svalbard, in the southwestern Nansen Basin (Fig. 1), where the research vessel R/V Lance was moored up to an ice floe for eight days.

The sea ice cover in the area is generally dominated by first- or second-year ice with only moderate amounts of deformation (Renner et al., 2013). While large seasonal variability exists in the area, summer ice thickness has been fairly stable since 2007. However, Renner et al. (2013) found further

220 indicators for a trend towards younger sea ice in the region. Little deformation and dominance of young ice leads to relatively low sea ice surface roughness, with a root mean square height of around or less than 0.1 m in the region (Beckers et al., 2015). Substantial snow cover can accumulate during spring, however, during the summer season, the snow melts completely contributing to extensive melt pond formation.

225 **3.2 Data set**

In situ and helicopter-borne measurements from ICE2012 are combined with four high-resolution TerraSAR-X (TS-X) satellite scenes. The satellite scenes are StripMap mode acqusitions, with a HH-VV channel combination (see Table 1 and Fig. 1). The scene labeled T1 was acquired in descending orbit, while T2-T4 were acquired in ascending orbits. All scenes were converted to ground range and

230 radiometrically calibrated to σ^0. The calibration was performed both with and without subtraction of the noise equivalent σ^0 (NESZ). For comparison with f_{MP} retrieved from helicopter-borne data, the scenes were geocoded with ESA's Sentinel-1 toolbox, SNAP (European Space Agency, 2016). All analysis were, however, performed in SLC range and azimuth coordinates. Open water areas were not included in our study. For each satellite scene, these areas were masked out with a simple binary

235 mask. The mask was created by filtering the scenes with a 13×13 pixels averaging sliding window, and manually setting a lower sea ice threshold value on σ^0_{HH} in each scene (-18 dB,-17 dB,-16 dB and -18 dB, for T1-T4 respectively). Regions with less than 750 pixels ($\sim 5000\ m^2$) were merged into the surrounding region (open water or sea ice) to smooth the mask.

A stereocamera system (ICE stereocamera system) was mounted in a single enclosure outside the

240 helicopter during ICE2012 (Divine et al., 2016, in review). The system consisted of two cameras (Canon 5D Mark II), combined with GPS/INS (Novatel) and a laser altimeter. f_{MP} was retrieved from downward-looking images captured by one of the cameras during five helicopter surveys performed between 31 July and 2 August 2012 (see Table 2 and Fig. 1). The footprint of the images was about 60×40 m for a typical flight altitude of about 35 m, and the images were not overlapping.

245 A full description of the method is given in Divine et al. (2015). In our study, f_{MP} was calculated from the processed images without sea water fraction (~ 5700 images), to better match the sea ice mask. This excluded melt pond fractions from the ice edges and small floes, resulting in a slightly higher f_{MP} than that obtained in Divine et al. (2015).

The ICE stereocamera system was also used to investigate sea ice surface topography at the floe

250 where R/V Lance was anchored. For this purpose, the cameras shot sequentially with a frequency of 1 Hz to ensure sufficient overlap between subsequent images during the flights. Using photogrammetric technique, the sequences of overlapping images were used to construct a digital terrain model

(DTM) of the sea ice surface. DTMs were generated for five selected segments of the ICE12 ice floe with a spatial resolution of 2 cm. Surface roughness, in form of root mean square height of the sea ice surface (s_{RMS}), was estimated from the DTMs using random sampling to account for spatial auto-correlation. Only grid nodes above the water level were used. The accuracy of the retrieved s_{RMS} were ± 4 cm according to *in situ* measurements from two test areas. A full description of the method is given in Divine et al. (2016, in review).

An automatic weather station located at the floe where R/V Lance was moored during ICE2012 measured wind speed and air temperature 2 m above the sea ice surface(Hudson et al., 2013). Wind speed (U_2) was measured with a three-dimensional ultrasonic anemometer (Campbell Scientific Inc., CSAT3), and air temperature was measured with a temperature probe (Vaisala, HMP155) in an unventilated radiation shield. Tab. 1 presents air temperature and 10 minutes averaged wind speed at the time of the satellite acquisitions.

3.3 Design of study

An easy recognizable sea ice floe present in two of the investigated satellite scenes (T3 and T4) is the main focus of our study (see Fig. 2). The floe had a diameter of ~ 3.6 km, and a collection of 43 images was captured across the floe during the 2$^{\text{nd}}$ helicopter flight on 2 August 2012 (see Tab. 2). The time offset between the flight and acquision of T4 was ~ 40 minutes. The position of the helicopter images had to be corrected for sea ice drift to retrieve co-location between the images and the floe captured in T4. As a first step, the image center coordinates were shifted according to drift information from GPS tracks of R/V Lance, positioned ~ 25 km south of the floe at the time of acquisition. Second, the track was manually adjusted by fitting the helicopter images with ground features, such as ice edges and areas with open water. Co-location of the helicopter images and the floe in T3 was based on the one of T4. The maximum error of the co-location was estimated to be 7 m lengthwise and crosswise the flight direction, resulting in a maximum possible areal offset of 27% between the satellite scene and each helicopter image. After co-location, mean and standard deviation of the polarimetric SAR features were calculated for the pixels underlying each of the helicopter images.

The statistical dependence between the extracted SAR features and the corresponding f_{MP} retrieved from each of the 43 helicopter images was evaluated with the non-parametric Spearman's rank correlation coefficient (r). For a sample size of n images, r is defined as

$$r = 1 - \frac{6 \sum d_i^2}{n(n^2 - 1)}, \tag{15}$$

where d_i is the difference in paired rank number i (Corder and Foreman, 2009). Rank ties are assigned a rank equal to the average of their position in the ascending order of the values. The coefficient takes values between -1 and 1, where values of ± 1 correspond to full correlation, while 0 corresponds to no correlation. A negative sign indicates an inverse relationship. The calculation of r

assumes of a monotonic relationship, and is less sensitive to outliers than Pearson's linear correlation
coefficient.

290   Two empirical models were proposed from the correlation results, representing an intermediate
and a low-wind case. A least squares linear fit with bisquare weights was used to construct the
models (Hoaglin et al., 1983). The models were applied to the full area of the floe in T3 and T4,
and to the full area of the four satellite scenes included in the study (T1-T4). The estimated f_{MP}
distributions were compared and evaluated towards the global empirical f_{MP} distribution retrieved

295   from the helicopter flights included in the study (see bottom entries Tab. 2). Scale sensitivity was
tested by using a range of different smoothing window sizes (13×13 to 51×51 pixels) in the f_{MP}
estimation.

4   Results

4.1   Sea ice conditions

300   During the ICE2012 campaign, regular sea ice thickness and melt pond surveys were performed on
the ice and from helicopter. Modal ice thickness in the region was less than in previous years with 0.7
to 0.9 m (Divine et al., 2015). The very close drift ice was fairly level with less than 10% deformed
ice. Sea ice surface roughness retrieved from the floe by R/V Lance is given in Table 3. The surface
roughness values are expected to be representative for the whole study region, as the sea ice in the

305   area was found to be very uniform (Hudson et al., 2013; Divine et al., 2015). The values also agree
well with values derived from laser altimeter observations by Beckers et al. (2015).

    At the time of the campaign, all snow had melted and extensive networks of melt ponds led to an
average f_{MP} of 26% of the sea ice area (Divine et al., 2015). The melt ponds were mostly whithin
15 to 30 cm deep, however, extensive melt led to some ponds having melted through the ice slab.

310   The water in the pond networks was therefore mostly saline.

    Hudson et al. (2013) report an average thinning of the sea ice next to R/V Lance of over 17 cm
between 28 July and 2 August which to a large degree can be explain by absorption of atmospheric
and oceanic heat by the ice. Air temperatures were mostly around freezing point varying only little
between -1 to $1.5°C$. Meteorological conditions were dominated by heavy cloud cover with only

315   short spells of incomplete or thin cloud cover. Ice cores were taken every other day between 27 July
and 2 August with an additional core on 28 July for chemical analysis. They confirm the presence of
a consistent 4 to 5 cm thick surface scattering layer of white, granular, deteriorated ice. Temperature
profiles through the ice were fairly stable with vertical variations between near $0°C$ at the surface
to -1 to $-1.3°C$ at the bottom. Salinity measurements show very low values in the upper 20 cm

320   with salinities of less than 1 psu and increasing to 3 to 4 psu near the bottom, in agreement with the
advanced stage of melt of the ice cover.

4.2 Correlation between polarimetric SAR features and f_{MP}

Correlation coefficients (r) between f_{MP} retrieved from the 43 helicopter images of the investigated floe, and the mean and standard deviation of the polarimetric SAR features extracted from

325 the corresponding areas in scenes T3 and T4, are presented in Table 4. Values significant within a 95% confidence interval are highlighted in bold, and values in parentheses show results after NESZ subtraction of the signal was included in the calibration. In scene T3, $R_{VV/HH}$ shows the strongest correlation to f_{MP}, both with and without NESZ subtraction. In addition, the mean of α_1 is significantly correlated to f_{MP} when the NESZ subtraction is included in the calibration. None of the

330 other investigated SAR features are significantly correlated to f_{MP} in scene T3. In scene T4, the mean values of most of the features, and some of their standard deviation values are correlated to f_{MP}. The strongest correlation is found between σ^0_{VV} and f_{MP}. Introducing NESZ subtraction in the calibration, however, reduces the number of correlations, indicating that the signal is close to, or reaching the noise floor.

335 Figure 3 confirms the low signal-to-noise ratio in T4. We show the 10, 25, 50, 75 and 90 percentiles of σ^0_{HH} (dB) and σ^0_{VV} (dB) retrieved for four different f_{MP} intervals on the floe present in scene T3 (top) and T4 (bottom), combined with the noise floor of the HH and VV channels. In T3, less than 10% of the signal is below the noise floor (~ -25 dB). Both σ^0_{HH} and σ^0_{VV} are increasing with f_{MP}. σ^0_{VV} has the steepest increase, confirming an increase in $R_{VV/HH}$ with f_{MP} (Tab. 4). In scene T4,

340 the backscatter signal is weaker and noise floor is higher than in scene T3 (~ -21 dB), both due to the higher incidence angle of scene T4 (see Tab. 1). This brings as much as 25% of the signal below the noise floor. The strength of the signal decreases with f_{MP}, implying specular reflection from the melt ponds, supported by the low wind speed (0.6 m/s) at acquisition of scene T4 (see Tab. 1). The difference between σ^0_{HH} and σ^0_{VV} is decreasing with f_{MP}, confirming an inverse relation between

345 $R_{VV/HH}$ and f_{MP} in T4 (Tab. 4). In scene T1 and T2, the noise floors are ~ 23 dB, leaving $\sim 15\%$ of the signal below the noise floor.

The melt ponds affect the polarimetric signatures in scene T3 and T4 differently (Table 4 and Fig. 3), mainly due to different wind conditions, but also due to different incidence angles and noise floors. Based on these results, two empirical models for f_{MP} estimation are presented in the

350 following. One model is retrieved from the intermediate-wind case seen in cene T3, and one from the low-wind case seen in scene T4.

4.3 Intermediate-wind case

In the intermediate-wind case of scene T3, $R_{VV/HH}$ was found to be the SAR feature with the strongest correlation to f_{MP}. Combining f_{MP} retrieved from the 43 helicopter images covering

355 the investigated floe with $R_{VV/HH}$ extracted from the corresponding areas in scene T3, we see an increase in $R_{VV/HH}$ with f_{MP} in Fig. 4, as well as a large variability between the samples. The

partly negative values of $R_{VV/HH}$ implies that $\sigma^0_{HH} > \sigma^0_{VV}$, especially in the areas with low f_{MP}. From visual inspection of the helicopter images, some of the lowest $R_{VV/HH}$ values origin from slightly deformed areas with a surface roughness possibly exceeding the Bragg criterion. A robust least squares linear fit was used to construct an empirical model from the displayed relationship:

$$f_{MP}(R_{VV/HH}) = 0.49 \cdot R_{VV/HH}(dB) + 0.30. \tag{16}$$

The goodness of fit of the model is reflecting large sample variation, with $r^2 = 0.21$ and $RMSE = 0.40$, but the model still provides a starting point for estimation of f_{MP}.

Applying the model based on Eq. 16 to the full floe in scene T3 results in the model probability density distributions (PDFs) presented in the top panel of Fig. 5. The results are presented both for a 21×21 and a 51×51 pixels smoothing window. Empirical distributions of f_{MP} retrieved from the 43 images covering the floe (floe) and from images in all included flights (global), are also included in the figure. Statistics of the distributions are given in Tables 2 and 5. The empirical global distribution has a slightly higher mean than the empirical floe distribution. Due to the few samples of the floe distribution, we consider the global distribution more appropriate for comparison with the modeled distributions. Employing the model with a 21×21 pixels smoothing window, equaling the areal size of the helicopter images, results in a mean close to the global empirical. The modeled distribution is however too wide compared to the empirical ones, reflecting the large sample variation seen in Fig. 5. Speckle (noise like interference between scatterers within a resolution cell) in the SAR image might explain the wider distribution. Increasing the smoothing window size reduces speckle, and a better correspondence between the width of the modeled and empirical distributions is achieved by employing a 51×51 pixels window. The bottom panel of Fig. 5 displays f_{MP} estimated for the floe in T3 based on eq.16 with a 51×51 pixels window. Open water is masked out. The estimation shows a highly spatially variable f_{MP}, with few homogenous areas. Areas of deformed sea ice displayed with bright colors in Fig. 2 cannot be recognized, even if these areas are expected to have a lower melt pond fraction. A further validation of the results is not possible based on the collected data.

Applying the intermediate-wind model with a 51×51 pixel window to the four full SAR scenes included in our study reveals a high correlation between the modeled and the empirical global f_{MP} distribution for T3 (see Fig. 6 and Tables 2 and 5). On the full scene scale, the model manages to reproduce both the mean and the standard deviation of the global distribution representative for the area. Scene T1 and T2 are acquired at $\sim 8°$ higher incidence angle than scene T3, and f_{MP} is slightly overestimated in these scenes. From Fig. 6, the overestimation is lower for scene T1 than for T2, possibly reflecting the low wind speed at acquisition of T1 (Tab 1). The least consistency between model and empirical distribution is, as expected, found for scene T4, confirming the results shown in Table 4 and Fig. 3.

4.4 Low-wind case

In the low-wind case of scene T4, σ_{VV}^0 was found to have the strongest correlation to f_{MP} among the investigated SAR features. Combining f_{MP} retrieved from the 43 helicopter images covering the floe with σ_{VV}^0 extracted from the corresponding areas in T4, we see a decrease in σ_{VV}^0 with f_{MP} in Fig. 7. As for the intermediate wind case, an empirical model was constructed using a robust least square linear fit to describe the relationship:

$$f_{MP}(\sigma_{VV}^0) = -0.32 \cdot \sigma_{VV}^0 (dB) - 4.64 \tag{17}$$

Again, the goodness of fit of the model reflects the high sample variability in Fig. 7, with $r^2 = 0.15$ and $RMSE = 0.63$, but we consider the model to provide a good starting point for estimation of f_{MP}.

Modeled PDFs based on eq. 17 for the full floe in scene T4 are presented in the top panel of Fig. 8 together with empirical distributions from the floe and from all flights included in the study. The modeled distributions give a good reproduction of the empirical mean (see Tables 2 and 5). As in the intermediate-wind case, a smoothing window of 51×51 pixels results in a distribution width closer to the empirical than a 21×21 pixels window. The σ_{VV}^0-based estimation of f_{MP} with a 51×51 smoothing window for the full floe in scene T4 result in a large spatial variability in f_{MP} (see bottom panel of Fig. 8). In contrast to the f_{MP} estimation based on $R_{VV/HH}$ for the floe in scene T3 (Fig. 5), the low-wind model partly manages to produce lower melt pond fraction in areas with deformed sea ice.

Investigating the low-wind model's capacity of estimating f_{MP} in the 4 full satellite scenes included in the study reveals that it is only applicable to give a good estimate in scene T4 (see Fig. 9 and Table 2 and 5)). In the three other scenes, it underestimates f_{MP}, and also introduces negative fractions. An underestimation is expected for lower incidence angles, as σ_{VV}^0 decreases with incidence angle, but the magnitude of the underestimation is too large to be explained by the incidence angle dependency alone.

5 Discussion

The results of this study show that retrieval of f_{MP} from X-band SAR is possible, but as in C-band, parameters like wind speed, incidence angle, surface roughness, and SAR scale and resolution will affect the interpretation of the polarimetric melt pond signature of an X-band SAR scene.

Accurate information about wind speed at the time of scene acquisition is crucial in f_{MP} retrieval from SAR. In scene T3, the intermediate wind speed at acquisition ($U_2 = 6.2$ m/s) allowed for backscatter from the melt ponds, making use of $R_{VV/HH}$ for f_{MP} estimation possible. Scharien et al. (2014b) finds that the Bragg criterion is exceeded for melt ponds at wind speeds above $U_{10} = \sim 5$ m/s in X-band, reducing the expected correlation between $R_{VV/HH}$ and f_{MP} above this

425   wind speed. This indicates that even better results could be achieved at lower wind speeds, but it also
leaves a very narrow wind speed interval for melt pond retrieval with X-band SAR. Scene T4 represents a low wind speed situation ($U_2 = 0.6$ m/s), and our results indicate specular reflection from
the melt ponds in this case, disrupting the use of polarimetric SAR features for melt pond estimation
as the melt pond signal is too weak. This is in agreement with findings in Scharien et al. (2012,

430   2014b). However, the lack of backscatter from the melt pond surfaces compared to the sea ice could
potentially be used for f_{MP} retrieval utilizing σ^0. This is confirmed by Han et al. (2016), suggesting
σ^0 to be a key feature in f_{MP} estimation for MYI in X-band during calm winds. On the other hand,
our results deviate from findings in C-band, where no correlation was found between σ^0_{HH} and f_{MP}
at low wind speeds by Yackel and Barber (2000).

435   Medium to high incidence angles ($> 35°$) have been found most suitable for $R_{VV/HH}$-based
retrieval of f_{MP} in C-band (Scharien et al., 2012, 2014b). In our study we found a significant correlation between $R_{VV/HH}$ and f_{MP} at an incidence angle of $29°$ (T3), indicating that lower incidence
angles might be used for f_{MP} estimation, at least in X-band. Scene T1 and T2 are acquired at
higher incidence angles ($36.9°$ and $37.9°$) than T3. In these two scenes, f_{MP} is overestimated by

440   the $R_{VV/HH}$-based model developed for scene T3. This is consistent with Scharien et al. (2014b),
showing an increase in $R_{VV/HH}$ with increasing incidence angle in C-band. The difference in modeled f_{MP} between scene T1 and T2 is most likely related to the low wind speed in T1, which is
below the expected wind speed limit for f_{MP} estimation based on $R_{VV/HH}$ in both C and X-band
(Scharien et al., 2012, 2014b). At an incidence angle of $44°$, a considerable part of the backscatter

445   signal was below the noise floor in our study. The low signal-to-noise ratio of TerraSAR-X limits
f_{MP} retrieval based on $R_{VV/HH}$ at high incidence angles, leaving the suitable range of incidence
angles smaller than for Radarsat -2 (Scharien et al., 2014a). The accuracy of f_{MP} estimation based
on σ^0_{VV} is also strongly dependent on incidence angle, as σ^0_{VV} in general decreases with increasing
incidence angle for sea ice. The underestimation of f_{MP} in scenes T1-T3, can partly be explained by

450   lower incidence angles, but the higher wind speeds at acquisition of these scenes likely also prevent
good estimates of f_{MP} based on σ^0_{VV}.

   The Brag criterion ($ks < 0.3$) is exceeded when $s_{RMS} > 1.4$ mm in X-band. The surface roughness estimations performed during the ICE2012 campaign indicates that the sea ice in the study
region exceeds this criterion, introducing a roughness dependency of $R_{VV/HH}$. This is in agreement

455   with previous findings in the study region (Beckers et al., 2015), but deviates from findings reported
by Scharien et al. (2014b), where fast ice at the Central Canadian Archipelago partly filled the criterion in X-band. From the helicopter images, some of the very low $R_{VV/HH}$ values observed at the
investigated floe in scene T3 were from slightly deformed areas, possibly explaining the negative
ratios. However, no general trend in low $R_{VV/HH}$ values in deformed areas was found in our study.

460   Sea ice deformation may also contributed to the large sample variations observed in Fig. 4 and 7.

Detailed surface roughness measurements combined with f_{MP} observations are needed to further investigate the influence of sea ice surface roughness on f_{MP} based on $R_{VV/HH}$.

The smoothing window size used for direct comparison between f_{MP} retrieved from the helicopter images and the polarimetric SAR features was appointed by the areal coverage of the helicopter images in our study. However, a 40×60 m window (corresponding to 21×21 pixels) might not be the ideal scale of investigation. Advancing the empirical models suggested in our study to the full floe or full scenes with a larger window (51×51 pixels) gave better reproductions of the width of the f_{MP} distribution retrieved from the helicopter images. A larger window size reduces the amount of speckle in the SAR scenes, which probably explains the improvement. Even larger window sizes were used in Scharien et al. (2014a), estimating f_{MP} based on $R_{VV/HH}$ in a 7.5×7.5 km grid from C-band Radarsat-2. Opposite to this, Han et al. (2016) found a 15×15 pixels window to give the best estimate of mean f_{MP} based on a combination of several SAR features in a TerraSAR-X scene. In climate applications, f_{MP} estimation from a full scene is more applicable than estimation from small areas within the scene. The large sample variability observed in Fig. 4 might therefore be negligible, as long as the $R_{VV/HH}$-based model produces a good full scene estimate of the mean f_{MP}. A wider study of the influence of scale on SAR f_{MP} retrieval is needed in the future.

In addition to $R_{VV/HH}$, five other dual-polarimetric SAR features were included in our study. The statistical feature RK showed a promising relation to f_{MP} in C-band on fast ice in the Fram Strait (Fors et al., 2015), but no relation was found in our investigation. Lack of the HV-channel, or less dominant height difference between ponds and sea ice could both possibly explain the absence of correlation. H' and α'_1 were found significantly correlated with f_{MP} in scene T4 and T3, respectively. In scene T4, the correlation to H' disappeared when NESZ subtraction was included in the calibration. This indicates that the correlation only reflected the low signal-to-noise ratio of the scene, as has previously been described in oil/water discrimination (Minchew et al., 2012). In scene T3, the correlation between f_{MP} and α'_1 is likely a result of the expected relation between α'_1 and $R_{VV/HH}$ (van Zyl and Kim, 2011). The correlations found between f_{MP} and mean and standard deviations of $|\rho|$ and $\angle\rho$ in scene T4 are, as for H', most likely related to the low wind speed and low signal-to-noise ratio of the scene. $|\rho|$, $\angle\rho$ and α'_1 were found important for f_{MP} retrieval in the X-band SAR scene investigated by Han et al. (2016), but lack of exact wind information in the study prevent a further comparison to our results.

6 Conclusions

Melt ponds play an important role in the sea-ice-ocean energy budget, but the evolution of melt pond fraction (f_{MP}) through the melt season is poorly monitored. Satellite-borne polarimetric SAR has shown promising results for f_{MP} retrieval in C-band, but few studies have investigated the opportunities in X-band. In this study we demonstrate a significant relation between f_{MP} and polarimetric

SAR features on drifting FYI in X-band, based on helicopter-borne images of the sea ice surface combined with four dual polarimetric SAR scenes. The study reveals a potential for f_{MP} estimation from X-band SAR, but also stresses the importance of including wind speed and incidence angle in a prospective robust f_{MP} retrieval algorithm. In the future, f_{MP} retrieved from X-band SAR could

500   supplement optical methods, and be used as a tool in climate applications, both as input in climate models and in studies of melt evolution mechanisms.

$R_{VV/HH}$ was found to be the most promising SAR feature for f_{MP} estimation in our study, in agreement with previous findings in C-band. The theoretical range of suitable wind speeds (< 5 m/s) and sea ice surface roughnesses ($s_{RMS} < 1.4$ mm) for f_{MP} extraction based on $R_{VV/HH}$ are

505   slightly more limited in X-band than in C-band, but our results show that one can use $R_{VV/HH}$ for f_{MP} estimation even if these criteria are partly exceeded. The high noise floor of TerraSAR-X also restricted use of scenes with incidence angles above $\sim 40°$, while an incidence angle of $29°$ gave good results. At very low wind speeds (0.6 m/s), the backscatter signal from the melt ponds became too low for f_{MP} retrieval based on $R_{VV/HH}$. In that case, σ^0_{VV} was found suitable for f_{MP}

510   estimation. All in all, use of X-band scenes can increase the total amount of SAR data accessible for f_{MP} retrieval, despite their limitations compared to C-band scenes.

An extended amount of *in situ* and airborne measurements together with satellite scenes are needed to establish robust f_{MP} estimation algorithms for X-band SAR. Information about wind speed is crucial for f_{MP} retrieval, and can be retrieved from existing meteorological models or au-

515   tonomous buoys measuring wind speed, where no ship or camp is present. Co-location of airborne observations and SAR imagery challenged coordinated use of existing data in our study. A possible offset in location between the helicopter images and the investigated SAR scenes represents a major source of uncertainty in our results, possibly introducing too low correlation values and a large RMSE of the empirical models. Better co-location, for instance through corner reflectors or

520   GPS senders located in the specific study area, should be aimed for in future studies. With a shift towards more seasonal drifting FYI, it is important to include this sea ice type in the studies, despite difficulties in comparing *in situ* and airborne measurements with satellite SAR scenes during drift.

Our study only investigates a few SAR scenes under similar sea ice conditions, and the ability of the suggested models to predict changes in f_{MP} is not included. This is an important aspect.

525   Future studies should aim to include a larger number of satellite scenes acquired during various sea ice conditions, melt pond evolution stages, wind speeds and incidence angles. The effect and limitations of sea ice surface roughness and dependency on filtering size and scale should also be further investigated.

Acknowledgements. The authors would like to thank the captain, crew and scientists from the Norwegian Po-

530   lar Institute (NPI) and Airlift AS on-board R/V Lance during ICE2012 for support and data collection. The TerraSAR-X data are provided by InfoTerra. We acknowledge S. Hudson at NPI for help with meteorological

data, and A. Fransson, also at NPI, for providing ice core information. Thanks to W. Dierking at the Alfred Wegner Institute and C. Brekke and T. Eltoft at Department of Physics and Technology, UiT-The Arctic University of Norway for participation in discussions, and to S. N. Anfinsen at Department of Physics and Technology,

535   UiT-The Arctic University of Norway for useful comments on the manuscript. The project was supported financially by Regional Differensiert Arbeidsgiveravgift (RDA) Troms County, by the project "Sea Ice in the Arctic Ocean, Technology and Systems of Agreements" ("Arctic Ocean", subproject "CASPER") of the Fram Center, and by Center for Ice, Climate and Ecosystems at the NPI.

References

540 Beckers, J. F., Renner, A. H. H., Spreen, G., Gerland, S., and Haas, C.: Sea-ice surface roughness estimates
from airborne laser scanner and laser altimeter observations in Fram Strait and north of Svalbard, Annals of
Glaciology, 56, 235–244, doi:10.3189/2015AoG69A717, 2015.

Cloude, S. R.: The dual polarisation entropy/alpha decomposition: A PALSAR case study, in: Proc. POLinSAR
2007, 22-26 Januar 2007, European Space Agency (ESA SP-644), Frascati, Italy, 2007.

545 Cloude, S. R. and Pottier, E.: An entropy based classification scheme for land applications of polarimetric SAR,
IEEE Transactions on Geoscience and Remote Sensing, 35, 68–78, doi:10.1109/36.551935, 1997.

Comiso, J. C. and Kwok, R.: Surface and radiative characteristics of the summer Arctic sea ice cover from multi-
sensor satellite observations, Journal of Geophysical Research, 101, 28 397–28 416, doi:10.1029/96JC02816,
1996.

550 Corder, G. W. and Foreman, D. I.: Nonparametric Statistics for Non-Statisticians: A Step-by-step approach,
John Wiley & Sons, Inc., Hoboken, USA, doi:10.1002/9781118165881, 2009.

Divine, D. V., Granskog, M. A., Hudson, S. R., Pedersen, C. A., Karlsen, T. I., Divina, S. A., Renner, A. H. H.,
and Gerland, S.: Regional melt-pond fraction and albedo of thin Arctic first-year drift ice in late summer,
Cryosphere, 9, 255–268, doi:10.5194/tc-9-255-2015, 2015.

555 Divine, D. V., Pedersen, C. A., Karlsen, T. I., Aas, H. F., Granskog, M. A., Hudson, S. R., and Gerland, S.:
Photogrammetric retrievals and analysis of small scale sea ice topography during summer melt, Cold Regions
Science and Technology, in review, 2016.

Donelan, M. A. and Pierson, W. J.: Radar scattering and equilibrium ranges in wind-generated waves with appli-
cation to scatterometry, Journal of Geophysical Research, 92, 4971–5029, doi:10.1029/JC092iC05p04971,

560 1987.

Doulgeris, A. P. and Eltoft, T.: Scale Mixture of Gaussian Modelling of Polarimetric SAR Data, EURASIP
Journal on Advances in Signal Processing, 2010, 1–13, doi:10.1155/2010/874592, 2010.

Drinkwater, M., Kwok, R., Rignot, E., Israelsson, H., Onstott, R. G., and Winebrenner, D. P.: Potential Ap-
plications of Polarimetry to the Classification of Sea Ice, in: Microwave Remote Sensing of Sea Ice, edited

565 by Carsey, F. D., vol. 68 of *Geophysical Monograph Series*, pp. 419–430, American Geophysical Union,
Washington, DC, USA, doi:10.1029/GM068, 1992.

Ehn, J. K., Mundy, C. J., Barber, D. G., Hop, H., Rossnagel, A., and Stewart, J.: Impact of horizontal spreading
on light propagation in melt pond covered seasonal sea ice in the Canadian Arctic, Journal of Geophysical
Research, 116, C00G02, doi:10.1029/2010JC006908, 2011.

570 Eicken, H., Grenfell, T. C., Perovich, D. K., Richter-Menge, J. A., and Frey, K.: Hydraulic controls of summer
Arctic pack ice albedo, Journal of Geophysical Research, 109, C08 007, doi:10.1029/2003JC001989, 2004.

Eom, H. J. and Boerner, W.-M.: Statistical properties of the phase difference between two orthogonally polar-
ized SAR signals., Geoscience and Remote Sensing, IEEE Transactions on, 29, 182–184, 1991.

European Space Agency: Sentinel-1 toolbox - SNAP, http://step.esa.int/main/toolboxes/snap/, 2016.

575 Fetterer, F. and Untersteiner, N.: Observations of melt ponds on Arctic sea ice, Journal of Geophysical Research:
Oceans, 103, 24 821–24 835, doi:10.1029/98JC02034, 1998.

Flocco, D., Schroeder, D., Feltham, D. L., and Hunke, E. C.: Impact of melt ponds on Arctic sea ice simulations
from 1990 to 2007, Journal of Geophysical Research: Oceans, 117, doi:10.1029/2012JC008195, 2012.

Flocco, D., Feltham, D. L., Bailey, E., and Schroeder, D.: The refreezing of melt ponds on Arctic sea ice, Journal
580   of Geophysical Research: Oceans, 120, 647–659, doi:10.1002/2014JC010140, 2015.

Fors, A. S., Doulgeris, A. P., Renner, A. H. H., Brekke, C., and Gerland, S.: On the releation between polari-
metric synthetic aperture radar (SAR) features and sea ice melt pond fraction, in: Proc. IGARSS 2015, pp.
3441–3445, Milano, Italy, 2015.

Fors, A. S., Brekke, C., Doulgeris, A. P., Eltoft, T., Renner, A. H. H., and Gerland, S.: Late-summer sea
585   ice segmentation with multi-polarisation SAR features in C and X band, The Cryosphere, 10, 401–415,
doi:10.5194/tc-10-401-2016, 2016a.

Fors, A. S., Brekke, C., Gerland, S., Doulgeris, A. P., and Beckers, J. F.: Late Summer Arctic Sea Ice Surface
Roughness Signatures in C-Band SAR Data, IEEE Journal of Selected Topics in Applied Earth Observations
and Remote Sensing, 9, 1199–1215, doi:10.1109/JSTARS.2015.2504384, 2016b.

590   Hajnsek, I., Pottier, E., and Cloude, S. R.: Inversion of surface parameters from polarimetric SAR, IEEE Trans-
actions on Geoscience and Remote Sensing, 41, 727–744, doi:10.1109/TGRS.2003.810702, 2003.

Han, H., Im, J., Kim, M., Sim, S., Kim, J., Kim, D.-J., and Kang, S.-H.: Retrieval of Melt Ponds on Arc-
tic Multiyear Sea Ice in Summer from TerraSAR-X Dual-Polarization Data Using Machine Learning Ap-
proaches: A Case Study in the Chukchi Sea with Mid-Incidence Angle Data, Remote Sensing, 8, 57,
595   doi:10.3390/rs8010057, 2016.

Hoaglin, D. C., Mosteller, F., and Tukey, J. W.: Understanding robust and exploratory data analysis, John Wiley
& Sons, Inc, New York, 1983.

Holland, M. M., Bailey, D. A., Briegleb, B. P., Light, B., and Hunke, E.: Improved sea ice shortwave radiation
physics in CCSM4: The impact of melt ponds and aerosols on Arctic sea ice, Journal of Climate, 25, 1413–
600   1430, doi:10.1175/JCLI-D-11-00078.1, 2012.

Howell, S. E. L., Tivy, A., Yackel, J. J., and Scharien, R. K.: Application of a SeaWinds/QuikSCAT sea ice
melt algorithm for assessing melt dynamics in the Canadian Arctic Archipelago, Journal of Geophysical
Research: Oceans, 111, doi:10.1029/2005JC003193, 2006.

Hudson, S. R., Granskog, M. A., Sundfjord, A., Randelhoff, A., Renner, A. H. H., and Divine, D. V.: Energy
605   budget of first-year Arctic sea ice in advanced stages of melt, Geophysical Research Letters, 40, 2679–2683,
doi:10.1002/grl.50517, 2013.

Inoue, J., Curry, J. A., and Maslanik, J. A.: Application of Aerosondes to Melt-Pond Observations over Arctic
Sea Ice, Journal of Atmospheric and Oceanic Technology, 25, 327–334, doi:10.1175/2007JTECHA955.1,
2008.

610   Istomina, L., Heygster, G., Huntemann, M., Schwarz, P., Birnbaum, G., Scharien, R., Polashenski, C., Perovich,
D., Zege, E., Malinka, A., Prikhach, A., and Katsev, I.: Melt pond fraction and spectral sea ice albedo retrieval
from MERIS data - Part 1: Validation against in situ, aerial, and ship cruise data, Cryosphere, 9, 1551–1566,
doi:10.5194/tc-9-1551-2015, 2015.

Jeffries, M. O., Schwartz, K., and Li, S.: Arctic summer sea-ice SAR signatures, melt-season characteristics,
615   and melt-pond fractions, Polar Record, 33, 101–112, doi:10.1017/S003224740001442X, 1997.

Kern, S., Brath, M., and Stammer, D.: Melt Ponds as Observed with a Helicopter-Borne, Multi-Frequency
Scatterometer in the Arctic Ocean in 2007, in: Proc. of ESA Living Planet Symp., European Space Agency
(ESA SP-686), Bergen, Norway, 2010.

Kim, D. J., Hwang, B., Chung, K. H., Lee, S. H., Jung, H. S., and Moon, W. M.: Melt pond mapping with high-resolution SAR: The first view, Proceedings of the IEEE, 101, 748–758, 2013.

Lee, J.-S. and Pottier, E.: Polarimetric radar imaging: From basics to applications, CRC Press, Taylor and Francis Group, Boca Raton, FL, USA, 2009.

Light, B., Grenfell, T. C., and Perovich, D. K.: Transmission and absorption of solar radiation by Arctic sea ice during the melt season, Journal of Geophysical Research: Oceans, 113, doi:10.1029/2006JC003977, 2008.

Mäkynen, M., Kern, S., Rösel, A., and Pedersen, L. T.: On the Estimation of Melt Pond Fraction on the Arctic Sea Ice With ENVISAT WSM Images, IEEE Transactions on Geoscience and Remote Sensing, 52, 7366–7379, doi:10.1109/TGRS.2014.2311476, 2014.

Mardia, K. V.: Measure of multivariate skewness and kurtosis with applications, Biometrica, 57, 519—-530, 1970.

Markus, T., Cavalieri, D. J., Tschudi, M. A., and Ivanoff, A.: Comparison of aerial video and Landsat 7 data over ponded sea ice, Remote Sensing of Environment, 86, 458–469, doi:10.1016/S0034-4257(03)00124-X, 2003.

Minchew, B., Jones, C. E., and Holt, B.: Polarimetric Analysis of Backscatter From the Deepwater Horizon Oil Spill Using L-Band Synthetic Aperture Radar, IEEE Transactions on Geoscience and Remote Sensing, 50, 3812–3830, doi:10.1109/TGRS.2012.2185804, 2012.

Moen, M.-A., Doulgeris, A. P., Anfinsen, S. N., Renner, A. H. H., Hughes, N., Gerland, S., and Eltoft, T.: Comparison of feature based segmentation of full polarimetric SAR satellite sea ice images with manually drawn ice charts, The Cryosphere, 7, 1693–1705, doi:10.5194/tc-7-1693-2013, 2013.

Nicolaus, M., Katlein, C., Maslanik, J., and Hendricks, S.: Changes in Arctic sea ice result in increasing light transmittance and absorption, Geophysical Research Letters, 39, doi:10.1029/2012GL053738, 2012.

Perovich, D. K.: Aerial observations of the evolution of ice surface conditions during summer, Journal of Geophysical Research, 107, 8048, doi:10.1029/2000JC000449, 2002.

Perovich, D. K. and Polashenski, C.: Albedo evolution of seasonal Arctic sea ice, Geophysical Research Letters, 39, doi:10.1029/2012GL051432, 2012.

Perovich, D. K., Grenfell, T. C., Light, B., Elder, B. C., Harbeck, J., Polashenski, C., Tucker, W. B., and Stelmach, C.: Transpolar observations of the morphological properties of Arctic sea ice, Journal of Geophysical Research, 114, C00A04, doi:10.1029/2008JC004892, 2009.

Perovich, D. K., Meier, W. N., Tschudi, M. A., Farrell, S., Gerland, S., and Hendricks, S.: Sea ice [in Arctic Report Card 2015], http://www.arctic.noaa.gov/reportcard, 2015.

Polashenski, C., Perovich, D., and Courville, Z.: The mechanisms of sea ice melt pond formation and evolution, Journal of Geophysical Research, 117, C01 001, doi:10.1029/2011JC007231, http://doi.wiley.com/10.1029/2011JC007231, 2012.

Renner, A. H., Hendricks, S., Gerland, S., Beckers, J., Haas, C., and Krumpen, T.: Large-scale ice thickness distribution of first-year sea ice in spring and summer north of Svalbard, Annals of Glaciology, 54, 13–18, doi:10.3189/2013AoG62A146, 2013.

Rösel, A. and Kaleschke, L.: Comparison of different retrieval techniques for melt ponds on Arctic sea ice from Landsat and MODIS satellite data, Annals of Glaciology, 52, 185–191, 2011.

Rösel, A. and Kaleschke, L.: Exceptional melt pond occurrence in the years 2007 and 2011 on the Arctic sea ice revealed from MODIS satellite data, Journal of Geophysical Research: Oceans, 117,
660   doi:10.1029/2011JC007869, 2012.

Rösel, A., Kaleschke, L., and Birnbaum, G.: Melt ponds on Arctic sea ice determined from MODIS satellite data using an artificial neural network, The Cryosphere, 6, 431–446, doi:10.5194/tc-6-431-2012, 2012.

Scharien, R. K., Yackel, J. J., Barber, D. G., Asplin, M., Gupta, M., and Isleifson, D.: Geophysical controls on C band polarimetric backscatter from melt pond covered Arctic first-year sea ice: Assessment using high-
665   resolution scatterometry, Journal of Geophysical Research: Oceans, 117, doi:10.1029/2011JC007353, 2012.

Scharien, R. K., Hochheim, K., Landy, J., and Barber, D. G.: First-year sea ice melt pond fraction estimation from dual-polarisation C-band SAR – Part 2: Scaling in situ to Radarsat-2, The Cryosphere, 8, 2163–2176, doi:10.5194/tc-8-2163-2014, 2014a.

Scharien, R. K., Landy, J., and Barber, D. G.: First-year sea ice melt pond fraction estimation from dual-
670   polarisation C-band SAR – Part 1: In situ observations, The Cryosphere, 8, 2147–2162, doi:10.5194/tc-8-2147-2014, 2014b.

Schröder, D., Feltham, D. L., Flocco, D., and Tsamados, M.: September Arctic sea-ice minimum predicted by spring melt-pond fraction, Nature Climate Change, 4, 353–357, doi:10.1038/nclimate2203, 2014.

Skrunes, S., Brekke, C., and Eltoft, T.: Characterization of Marine Surface Slicks by Radarsat-2
675   Multipolarization Features, IEEE Transactions on Geoscience and Remote Sensing, 52, 5302–5319, doi:10.1109/TGRS.2013.2287916, 2014.

Tschudi, M. A., Maslanik, J. A., and Perovich, D. K.: Derivation of melt pond coverage on Arctic sea ice using MODIS observations, Remote Sensing of Environment, 112, 2605–2614, doi:10.1016/j.rse.2007.12.009, 2008.

680   van Zyl, J. J. and Kim, Y.: Synthetic Aperture Radar Polarimetry, John Wiley & Sons, Inc, Hoboken, USA, 2011.

Yackel, J. J. and Barber, D. G.: Melt ponds on sea ice in the Canadian Archipelago: 2. On the use of RADARSAT-1 synthetic aperture radar for geophysical inversion, Journal of Geophysical Research, 105, 22 061, doi:10.1029/2000JC900076, 2000.

685   Yackel, J. J., Barber, D. G., Papakyriakou, T. N., and Breneman, C.: First-year sea ice spring melt transitions in the Canadian Arctic Archipelago from time-series synthetic aperture radar data, 1992–2002, Hydrological Processes, 21, 253–265, doi:10.1002/hyp.6240, 2007.

Zege, E., Malinka, A., Katsev, I., Prikhach, A., Heygster, G., Istomina, L., Birnbaum, G., and Schwarz, P.: Algorithm to retrieve the melt pond fraction and the spectral albedo of Arctic summer ice from satellite
690   optical data, Remote Sensing of Environment, 163, 153–164, doi:10.1016/j.rse.2015.03.012, 2015.

Table 1. Overview of the satellite scenes.

Date	Time (UTC)	Scene ID	Incidence angle	Pixel spacing (az. × ground range)	Wind speed (2 m.a.s.)	Air temperature (2 m.a.s.)
28 Jul 2012	06:52	T1	36.9°	2.4 m × 1.5 m	1.6 m/s	0.1°C
29 Jul 2012	14:25	T2	37.9°	2.5 m × 1.5 m	5.1 m/s	1.1°C
31 Jul 2012	13:51	T3	29.4°	2.4 m × 1.9 m	6.2 m/s	−0.8°C
2 Aug 2012	14:51	T4	44.2°	3.0 m × 1.3 m	0.6 m/s	0.8°C

Table 2. Overview of the images captured during the helicopter flights. Only images without open water fraction are included in the study. The bottom entries show the global values derived from all five flights, and the local values of the floe investigated in T3 and T4.

Date	Time (UTC)	No. of images	Transect length	Mean f_{MP}	Std. f_{MP}
31 Jul 2012	7:36-8:10	848	67 km	30.1%	10.0%
1 Aug 2012	7:22-8:34	1364	139 km	31.1%	12.3%
1 Aug 2012	16:45-18:03	1383	154 km	34.8%	12.8%
2 Aug 2012	11:21-12:00	676	78 km	33.0%	13.7%
2 Aug 2012	14:43-16:04	1458	170 km	33.2%	11.4%
Global values	-	5729	608 km	33.2%	11.4%
Floe values	-	43	4 km	30.6%	11.1%

Table 3. Estimated sea ice surface roughness (s_{RMS}) from five segments at the floe by R/V Lance. Values in parenthesis displays standard deviations (std) of s_{RMS}.

Segment Nr.	Area	s_{RMS} $(std(s_{RMS}))$
1	11000 m^2	6.7 (0.3) cm
2	13530 m^2	11.0 (10) cm
3	11670 m^2	7.4 (0.6) cm
4	13820 m^2	9.0 (0.4) cm
5	12380 m^2	10.0 (0.4) cm

Table 4. Spearman's correlation coefficient (r) between f_{MP} retrieved from the helicopter images at the investigated floe, and mean and standard deviation of the polarimetric SAR features from the corresponding area in T3 and T4. Bold indicate significant values and values in parentheses are retrived after including NESZ subtraction in the calibration process.

SAR feature	r (T3) Mean	r (T3) Std.	r (T4) Mean	r (T4) Std.
σ^0_{HH}	0.05 (0.04)	0.09 (0.10)	**-0.32 (-0.33)**	-0.22 (-0.27)
σ^0_{VV}	0.21 (0.21)	0.09 (0.09)	**-0.53 (-0.54)**	**-0.52 (-0.54)**
$R_{VV/HH}$	**0.46 (0.45)**	-0.07 (0.03)	**-0.31 (-0.31)**	-0.01 (**-0.48**)
H	0.21 (0.11)	0.14 (0.25)	**0.45** (0.22)	0.07 (-0.17)
α_1	0.26 (**0.40**)	0.17 (0.00)	-0.18 (-0.24)	0.30 (0.11)
RK	0.03 (0.07)	0.04 (0.07)	0.04 (-0.15)	0.13 (0.08)
$|\rho|$	-0.22 (-0.13)	-0.00 (0.04)	**-0.40** (-0.17)	-0.06 (**-0.44**)
$\angle\rho$	0.01 (-0.14)	0.23 (0.10)	-0.10 (-0.08)	**0.55** (0.12)

Table 5. Statistics of modeled f_{MP} distributions.

Area	Window size (pixels)	$f_{MP}(R_{VV/HH})$ Mean	$f_{MP}(R_{VV/HH})$ Std.	$f_{MP}(\sigma^0_{VV})$ Mean	$f_{MP}(\sigma^0_{VV})$ Std.
T3, floe	21×21	34.9%	25.14%	-	-
T3, floe	51×51	35.0%	11.1%	-	-
T4, floe	21×21	-	-	32.4%	23.6%
T4, floe	51×51	-	-	31.9%	15.0%
T1, full scene	51×51	36.2%	12.6%	-6.1%	23.9%
T2, full scene	51×51	45.7%	13.6%	-19.5%	19.0%
T3, full scene	51×51	31.2%	11.3%	-32.6%	23.3%
T4, full scene	51×51	53.3%	13.5%	28.2%	14.0%
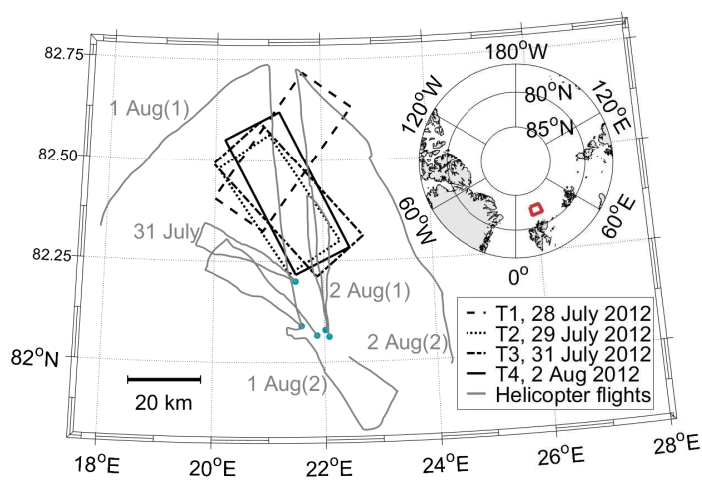
Figure 1. Map of the study area north of Svalbard, showing the location of the satellite scenes and the track of the helicopter flights. Blue dots mark the starting points of the flights. The red box in the inset map of the northern hemisphere shows the geographical position of the area displayed.
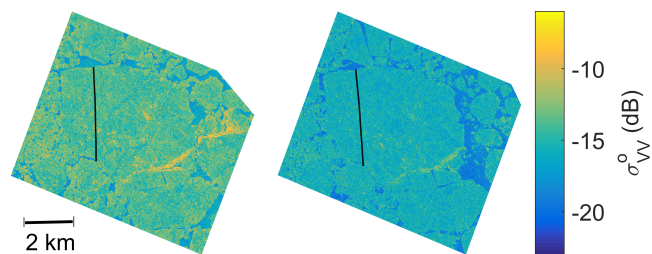
Figure 2. The floe investigated in scene T3 (left) and T4 (right). The black line marks the transect along which the helicopter image were taken.
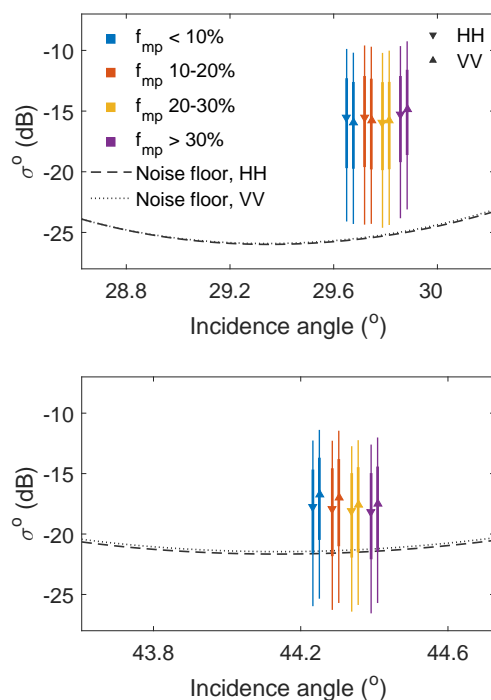
Figure 3. Signal-to-noise analysis of HH and VV channels for areas with different f_{mp} retrieved from the investigated floe in scene T3 (top) and T4 (bottom). The triangles displays the median of σ^0_{HH} (dB) (upward pointing) and σ^0_{VV} (downward pointing). The thin line represents the part of σ^0 falling between the 10 and the 90 percentile, while the thick line represents the part of σ^0 falling between the 25 and 75 percentile. Hence, the lines indicate the distributions. All markers are offset from the middle position for clarity.
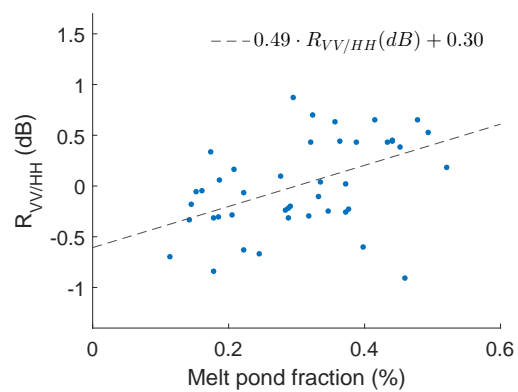
Figure 4. Scatter plot displaying f_{MP} retrieved from the 43 helicopter images covering the investigated floe in T3, and $R_{VV/HH}$ extracted from the corresponding areas. The trend line represents a robust bisquare weights least squares linear fit of the data.
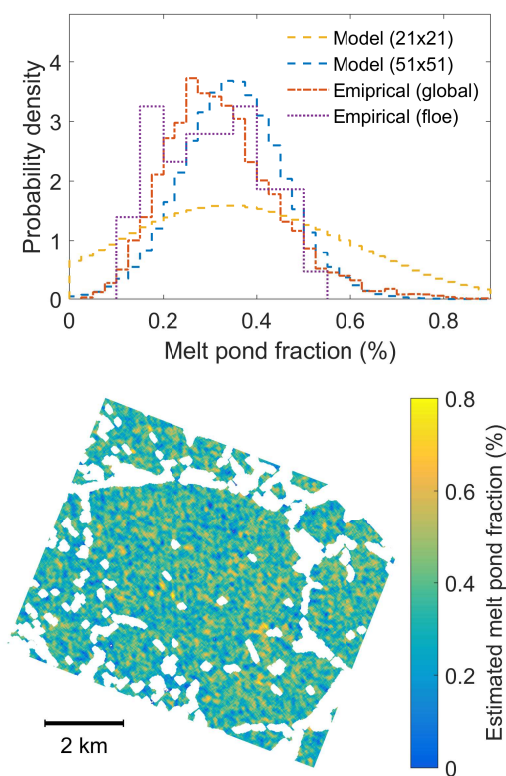
Figure 5. Top: Probability density distributions of f_{MP} for the investigated floe in T3. Curves represent distributions produced by the model based on $R_{VV/HH}$ with 21×21 and 51×51 pixels windows, and empirical distributions from all helicopter flights (global) and from the specific floe (floe). Bottom: Estimated f_{MP} from the $R_{VV/HH}$ based model with a 51×51 pixels window for investigated floe in T3.
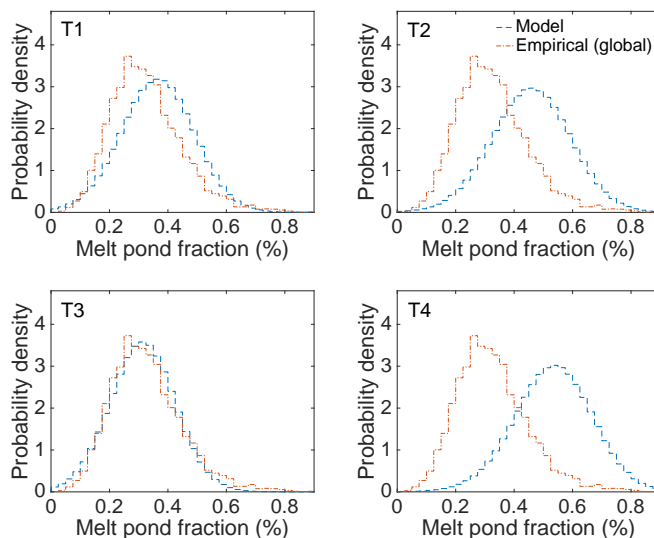
Figure 6. Probability density distributions of f_{MP} for the four investigated scenes (T1-T4). Curves represent distributions produced from the $R_{VV/HH}$ based model with a 51×51 pixels window, and the empirical distribution retrieved from all five helicopter flights.
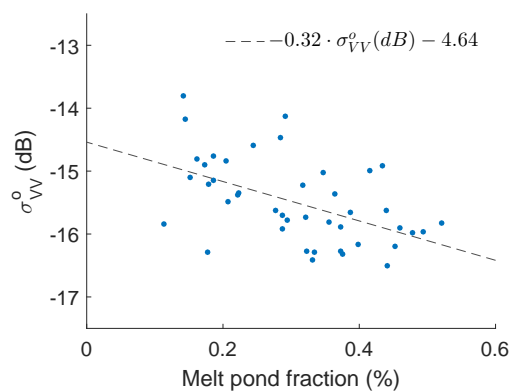
Figure 7. Scatter plot displaying f_{MP} retrieved from the 43 helicopter images covering the investigated floe in T4, and σ^0_{VV} extracted from the corresponding areas. The trend line represents a robust bisquare weights least squares linear fit of the data.
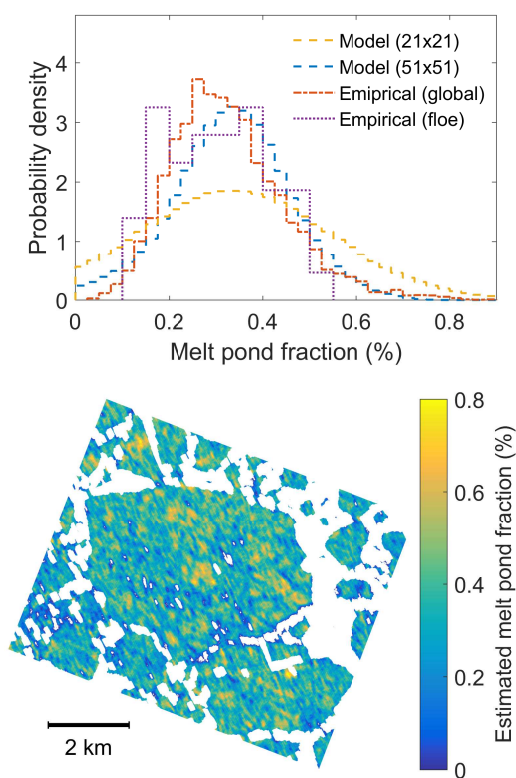
Figure 8. Top: Probability density distributions of f_{MP} for the investigated floe in T4. Curves represent distributions produced by the model based on σ^0_{VV} with 21×21 and 51×51 pixels windows, and empirical distributions from all helicopter flights (global) and from the specific floe (floe). Bottom: Estimated f_{MP} from the σ^0_{VV} based model with a 51×51 pixels window for investigated floe in T4.
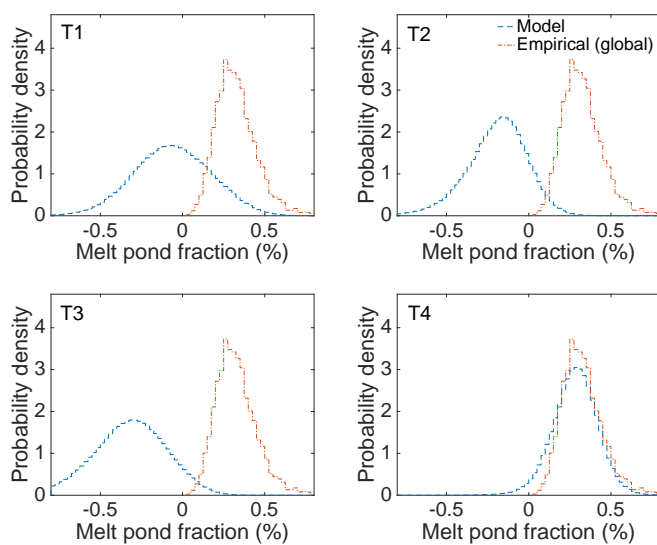
Figure 9. Probability density distributions of f_{MP} for the four investigated scenes (T1-T4). Curves represent distributions produced from the σ^0_{VV} based model with a 51×51 pixels window, and the empirical distribution retrieved from all five helicopter flights.